Earth and Planetary Science Letters 440 (2016) 178–186

Contents lists available at ScienceDirect

Earth and Planetary Science Letters

www.elsevier.com/locate/epsl

Iron spin state and site distribution in $FeAlO_3$-bearing bridgmanite

Chris E. Mohn [a,*], Reidar G. Trønnes [a,b]

[a] Centre for Earth Evolution and Dynamics, University of Oslo, N-0315 Oslo, Norway
[b] Natural History Museum, University of Oslo, N-0316, Norway

ARTICLE INFO

Article history:
Received 7 August 2015
Received in revised form 17 December 2015
Accepted 5 February 2016
Available online 23 February 2016
Editor: J. Brodholt

Keywords:
spin transition
density functional theory
ferric iron
bridgmanite
perovskite

ABSTRACT

DFT at the GGA, GGA + U and hybrid functional levels were used to investigate thousands of different Al and Fe^{3+} configurations of $MgSiO_3$–$FeAlO_3$ (MS–FA) and $MgSiO_3$–$FeAlO_3$–Al_2O_3 bridgmanite at deep mantle conditions. Comparison of the different functionals and atomic charge analysis suggests that GGA, frequently used to explain high to low spin transitions observed in several Mössbauer and X-ray emission spectroscopy experiments, is hampered by spurious self-interaction errors in the exchange-correlation energy. Configurational Boltzmann averaging shows that the B site is thermally inaccessible to Fe^{3+} at the GGA + U and hybrid levels, and we find no evidence for a spin-pairing transition in fully (thermodynamically) equilibrated samples of bridgmanite, even at the lowermost mantle conditions. The comparison of the cation radii of Fe^{3+} and Mg supports a spin transition accompanied by a site exchange, but the flexibility of Fe–O bonds to locally adapt promotes the incorporation of iron in the irregularly coordinated A-site. The concept of ionic radii is therefore unsuitable for analysis of spin state and site exchange in bridgmanite at these conditions. Consistent with previous computational work and experimental studies with glass and gel as starting material, we find that ferric iron kinetically trapped at the B site undergoes a spin transition under lowermost mantle conditions. In bridgmanite with mole fraction of Fe^{3+} > Al a charge-balancing amount of low spin Fe^{3+} will be thermodynamically stable at the B site, but because bridgmanite in peridotitic and basaltic lithologies mostly has Al/Fe_{total} above unity, FA with high spin Fe^{3+} in the A-site will be the dominant iron component. The lack of a Fe^{3+} spin transition in the FA-component has important implications for bridgmanite–ferropericlase partitioning of iron and magnesium and the mineral physics of the lowermost mantle.

1. Introduction

Perovskite-structured bridgmanite with $MgSiO_3$-dominated composition is the most abundant mineral in the Earth, constituting about 70% of the lower mantle. The ABO_3-structure includes an irregular and distorted 6 to 12 coordinated A site occupied by Fe^{2+}, Mg^{2+}, Fe^{3+} and minor Al^{3+} and a smaller octahedral B site, containing mainly Si^{4+} and Al^{3+} (Vanpeteghem et al., 2006). Experimental studies of natural peridotitic and basaltic compositions show that the atomic ratio Al/Fe_{total} of bridgmanite is mostly higher than unity (see references in Supplementary information). With cation sums normalized to 200, bridgmanite phases in mantle lithogies have average Al and Fe_{total} of 9 and 8 in peridotites and 37 and 25 in basalts, respectively. Peridotite assemblages do not include a separate aluminous phase, but majoritic garnet coexisting with bridgmanite in the uppermost regions of the lower mantle has the highest Al-contents of the two. Even with coexisting Al-rich phases in basaltic lithologies, the bridgmanite is Al-rich (and Fe-poor). Several experimental and computational studies have documented an energetic preference for the charge-coupled trivalent substitution of the end members $Al_AAl_BO_3$ and $Fe_AAl_BO_3$ to replace the $MgSiO_3$ component in bridgmanite, rather than vacancy assisted mechanisms (Walter et al., 2006; Li et al., 2005a; Brodholt, 2000), see also Supplementary information. A good fit for Fe^{3+} and aluminium in the A- and B-sites, respectively, explains the favourable energetics of this substitution.

Fe^{2+} is the predominant form of iron in the uppermost mantle ferrosilicates, olivine and pyroxene and fertile peridotites have FeO and Fe_2O_3 contents of about 8 and 0.2 wt%, respectively (Palme and O'Neill, 2003). Because the bulk composition of the convective mantle, including the oxygen content is roughly constant, the deeper part of the upper mantle and transition zone reaches saturation with Fe-dominated metal alloy due to the increasing proportion of increasingly majoritic garnet and to the incorporation of Fe^{3+} in this mineral (Rohrbach et al., 2007). The metal saturation is even more pronounced in the bridgmanite-dominated Fe^{3+}-rich assemblages of the lower man-

* Corresponding author.
E-mail address: chrism@geo.uio.no (C.E. Mohn).

http://dx.doi.org/10.1016/j.epsl.2016.02.010
0012-821X/

tle (Frost et al., 2004). We have therefore investigated bridgmanite compositions on the $MgSiO_3$–$FeAlO_3$ (MS–FA) join and in the $MgSiO_3$–$FeAlO_3$–Al_2O_3 (MS–FA–A_2) systems. The investigated compositions are 6.25% and 12.5% FA in the MS–FA system ($Mg_{1-x}Fe_xAl_xSi_{1-x}O_3$ with $X = 0.0625$ and $X = 0.125$) and 6.25% FA + 6.25% A_2 ($Mg_{1-2x}Fe_xAl_{3x}Si_{1-2x}O_3$ with $X = 0.0625$).

Pressure-induced spin transitions will influence the physical properties, like the equation of state and thermal conductivity of bridgmanite. Therefore, the electronic state and element distribution between the lattice positions provide important insights into the dynamics of the deep mantle. A spin-paring can take place in the deep mantle when the "spin pairing energy" is more negative than the energy associated with the splitting of the iron 3*d* bands. That is, pairing of electrons require additional energy to overcome Coulombic repulsions between electrons and compensating for loss in favourable exchange interactions between like spins. The breakdown of Hunds rule can be explained in the framework of crystal field theory by the increase in the splitting, χ, between the e_g and t_{2g} energy levels with decreasing Fe–O bond length and increasing pressure $\chi \sim R(Fe^{3+}\text{–}O)^{-5}$ (Hofmeister, 2006; Ohnishi, 1978). When the chemical bond is markedly covalent, however, a pressure induced spin transition is explained by an increasing overlap between the O 2*p* and metal 3*d* states, resulting in wider bands, which in turn favour spin-pairing (Cohen et al., 1997). If Fe^{3+} after spin-pairing is equal or smaller in size than Al^{3+}, the transition can be accompanied by the site-exchange $Fe^{3+}_{A,HS} + Al^{3+}_{B} \rightarrow Fe^{3+}_{B,LS} + Al^{3+}_{A}$ to reduce overall strain, but since the Fe–O bond is markedly covalent, the use of ionic radii to assign iron to a specific site can be highly misleading. A particular robust and popular method for measuring atomic radii in solids is that of a Bader-volume analysis, where the charge density is decomposed in individual contributions using a density minimum-surface criterion to separate atoms (Henkelman et al., 2006). The charge enclosed within this Bader volume is a good approximation to the total electronic charge of an atom.

Whereas Fe^{2+} in ferropericlase undergoes a transition to the low spin state in the lower half of the mantle (Badro et al., 2003; Wentzcovitch et al., 2009), various studies of the iron spin state in bridgmanite have yielded conflicting evidence. Some of the confusion between different experimental results stems from the uncertainties about the distribution of Fe^{3+} and Al between the A and B sites. Recent computational and experimental studies show that iron located at the B site undergoes a spin transition (Li et al., 2005b; Hsu et al., 2012; Huang and Pan, 2012; Catalli et al., 2010, 2011; Potapkin et al., 2013; Fujino et al., 2012, 2014; Kupenko et al., 2015). The GGA + U results of Hsu et al. (2012), however, show that $Fe^{3+}_{B,LS}$ is much higher in energy (>1 eV) than $Fe^{3+}_{A,HS}$ at lowermost mantle conditions, suggesting that high-spin ferric iron remains at the A site as long as $Al \geq Fe^{3+}$. This is in agreement with recent Mössbauer study of FA-bearing bridgmanite (Potapkin et al., 2013) and X-ray emission spectroscopy of FA-bearing silicate glass (Mao et al., 2014), where no spin transition was found, but contrasts with other experimental work (Catalli et al., 2010, 2011; Fujino et al., 2012, 2014) and conventional GGA calculations (Li et al., 2005b) carried out *without* the use a +U repulsion term. In these conventional GGA calculations, the energy difference between the $Fe^{3+}_{A,HS}$ and $Fe^{3+}_{B,LS}$ configurations was only 0.2 eV (within a 80 ion simulation box) at 100 GPa, which is $< k_B T$, indicating that *both* A and B sites are populated by ferric iron at pressures and temperature above 100 GPa and 3000 K. Since the GGA results are frequently used to explain high to low spin transition of ferric iron in several Mössbauer and X-ray emission spectroscopy experiments (Catalli et al., 2010, 2011; Fujino et al., 2012, 2014) we address the origin of the discrepancy between GGA and GGA + U.

The lack of agreement between the GGA and the GGA + U results may be surprising since conventional GGA reproduce many structural and thermodynamic properties of ferric-containing oxides, also those with a high concentration of iron, including α–Fe_2O_3 itself (Rollmann et al., 2004). However, the Self-Interaction Error (SIE) in the exchange-correlation term of GGA is associated with the spurious interaction of an electron with itself, which can be large in strongly correlated compounds. In cases where the electronic environment changes dramatically, such as for many redox reactions or pressure induced spin transitions, the SIE does not always cancel out. Adding a Hubbard +U term to the energy removes parts of this spurious self-interaction, favouring filling the 3*d* orbitals. This results in higher charge and smaller atomic radii, and can influence the relative stabilization of Fe^{3+}_{HS} vs. Fe^{3+}_{LS}, since a "GGA + U iron" could "fit" better within the small B-site compared to the somewhat larger "GGA iron". However, the Hubbard +U term is not perfect either (not uniquely defined) and depends on the charge, spin state and local oxygen neighborhood of a given iron, although recent implementation where the +U term has been calculated self-consistently, using linear response theory, appear more transferable across compositions and less sensitive to changes in local coordination (Cococcioni and de Gironcoli, 2005). The spin transition reported by Hsu et al. (2011) on the B-site of $(Mg, Fe)(Si, Fe)O_3$, where the +U was calculated self-consistently, is in good agreement with that obtained experimentally from Mössbauer analysis by Catalli et al. (2010).

The lack of agreement between different experimental and computational studies has motivated us to analyze the origin of the discrepancy in more detail, and we carry out additional calculations using state-of-the-art hybrid methods where the exchange-correlation contribution to the DFT energy was calculated using the screened Heyd–Scuseria–Ernzerhof (HSE06) functional where a fractional amount of exact Hartree–Fock (HF) exchange is added to the total energy (Heyd et al., 2003; Heyd and Scuseria, 2004). HSE06 reduces the SIE, and correctly describes the band gap of the notorious case of FeO, where conventional GGA fails (Alfredsson et al., 2004). For α–Fe_2O_3 (hematite), for example, it accurately predicts structural magnetic and electronic properties without using 3*d* electron-specific parameters such as the Hubbard +U term (Pozun and Henkelman, 2011).

We have previously shown how configurational Boltzmann averaging may be used to calculate thermodynamic properties at high pressure for different oxides such as ferropericlase (Mohn and Stølen, 2005) and various perovskite phases (Bakken et al., 2003; Mohn et al., 2005a). In these cases the site configurational entropy is far from that expected from an ideal solid solution model, since the species are markedly dissimilar i.e. they have different charge and/or size (Todorov et al., 2004; Stølen et al., 2006; Mohn et al., 2005b). Because the trivalent Fe and Al ions in bridgmanite are not distributed randomly over the A and B site (Li et al., 2005a; Hsu et al., 2012), we do not resort to the use of any ideal solid solution models but investigate a large number of individual cation arrangements, followed by an appropriate Boltzmann statistical analysis.

2. Theory

Configurational Boltzmann averaging involves 2 steps. First, we map the configurational space by distributing the Fe^{3+} and Al over both A and B sites within an orthorombic supercell constructed from the parent $MgSiO_3$ bridgmanite structure, followed by full free energy minimisations of the different configurations of Fe^{3+} and Al. Next, properties are calculated as Boltzmann averages over the free-energy minima associated with the distinct arrangements of Al and Fe^{3+} (with spin σ) at the electronic ground

state (Allan et al., 2001; Bakken et al., 2003; Todorov et al., 2004; Mohn et al., 2005b; Stølen et al., 2006). The ensemble average at temperature T of a microscopic property, Y, such as the enthalpy or volume, is given as

$$< Y >= \frac{\sum_{i=1}^{K_\sigma} Y_\sigma^i \exp(\frac{-G_\sigma^i}{k_B T})}{\sum_{i=1}^{K_\sigma} \exp(\frac{-G_\sigma^i}{k_B T})}. \quad (1)$$

The probability of finding the ensemble in a given atomic configuration i with spins σ is

$$p_\sigma^i = \frac{\exp(\frac{-G_\sigma^i}{k_B T})}{\sum_{i=1}^{K_\sigma} \exp(\frac{-G_\sigma^i}{k_B T})} \quad (2)$$

where i now runs over all distinct configurations of Al and Fe^{3+}. K_σ is the total number of free energy minima associated with distinct basin on the system free energy surface, k_B is Boltzmann's constant and Y_σ^i is the property of configuration i with spin σ.

In the equations above, G_σ^i is the minimised free-energy of configuration i with spin σ and is given as

$$G_\sigma^i = H_\sigma^i + \frac{1}{2}\sum_j \hbar\omega_j - T(S_{vib}^i + S_{mag}^i), \quad (3)$$

where H_σ^i is the static enthalpy of configuration i. The second term is the zero-point vibrational energy (j runs over the vibrational modes, ω_j), S_{vib}^i is the vibrational energy-contributions to G_σ^i and S_{mag}^i is the magnetic entropy contribution associated with the magnetic moments of the different iron-atoms. In general, the evaluation of the summation in Eq. (1) is exhaustive, and with the exception of the smallest simulation cells or compositions close to the dilute limit, efficient techniques for sampling the configurational space are required. In this work we use symmetry arguments by means of identifying symmetrically equivalent configurations of Fe^{3+} and Al, which reduces the overall cost in evaluating Eq. (1) (Mohn et al., 2005b).

3. Computational details

At the lowermost mantle conditions (e.g. 100 GPa and 3000 K), we are still within the valid regime of the quasi-harmonic approximation (Tsuchiya et al., 2005), and we can assume that the vibrational entropy of atomic configuration i is given as:

$$S_{vib}^i = k_B T \sum_j \ln(1 - \exp(-\hbar\omega_j / k_B T)). \quad (4)$$

We calculate S_{vib}^i for a range of atomic configurations (Togo et al., 2008), including extreme cases where all the iron (or aluminum) are clustered together within the first coordination shell or arranged as farthest neighbours. Results from these test-calculations show that S_{vib}^i is insensitive to configuration and the free energy difference between the configurations are $T * \Delta S_{vib}^i <$ 0.05 eV at $T \sim 3000$ K for bridgmanite with 6.25% and 12.5% FA.

Since we are mainly interested in free energy *differences* to calculate site and spin populations, we can ignore the vibrational contributions to the free energy. Furthermore, assuming that the spin micro-states at the *different* sites interact weakly (Ulbrich and Waldbaum, 1976), $S_{i,mag}$ in equation (3) can be written

$$S_{mag}^i = -k_B X_{Fe^{3+}} \sum_\sigma n_\sigma \ln(d_\sigma(2S_\sigma + 1)) \quad (5)$$

where S_σ and d_σ are the total spin and orbital degeneracy of the atomic configuration i (i.e. in an octahedral crystal field, $S = 1/2$ and $d_\sigma = 3$ for ferric iron in the LS-state; $S = 5/2$ and $d_\sigma = 1$ for ferric iron in the HS-state; $S = 3/2$ and $d_\sigma = 6$ for ferric iron in IS state). We compare the enthalpies of the antiferromagnetic and ferromagnetic ordering of 10 different atomic configurations, where two Fe^{3+} are distributed in our simulations box. The energy differences between antiferromagnetic and ferromagnetic ordering of iron atoms are less than 0.1 eV/80 ion supercell, confirming the validity of equation (5).

The energy minimisations are carried out by the full relaxations of the lattice-parameters, basic atomic positions and the cell volume at high, intermediate and low spin-configurations of Fe^{3+}. The orthorhombic $3 \times 3 \times 2$ (80-ion) supercell used in the calculations is constructed from the primitive orthorhombic 5-ion cell (space group Pbnm). All calculations reported are carried out in the static limit at 100 GPa, consistent with the total (static + thermal) pressure of about 127 GPa at 3000 K and 136 GPa at 4000 K.

The exchange correlation contribution to the DFT energy was calculated using the Vienna *ab initio* simulation program (Kresse and Joubert, 1999) at GGA, using the Perdew–Burke–Erntzerhof (PBE), functional (Perdew et al., 1996), GGA + U and HSE06 levels of theory. We use the same Hubbard Coulomb U parameter (U = 5 eV) as in previous computational studies of bridgmanite on the MS–FA join (Huang and Pan, 2012), which gives results in very good agreement with those of Hsu et al. (2012). In HSE06, the Coulomb kernel is decomposed into short- and long-range contributions, such that the exchange-correlation energy mimics that of hybrid PBE0 at short range, and GGA (PBE) at long range. An admixture of 0.25 Hartree–Fock exchange was used in the HSE06 calculations. Test calculations indicate that a constant plane-wave energy cut-off of 700 eV and a uniform $2 \times 2 \times 2$ Monkhorst–Pack grid were sufficient for the present purpose. Additional test-calculations were carried out using a larger 360-atom ($3 \times 3 \times 2$) cell constructed from the conventional (20-ion) unit cell. In these calculations only the Γ point were sampled in the Brillouin zone.

4. Results and discussions

4.1. Spin and site populations in bridgmanite from DFT

In Fig. 1 we report enthalpies and volumes of a range of individual atomic configurations at 100 GPa for bridgmanite with 6.25% FA. The atomic configurations are constructed by distributing a single pair of Fe^{3+} and Al over *both* A and B sites, followed by full structural optimisation of each individual configuration at the GGA and GGA + U levels of theory with LS, IS and HS iron. A selection of HSE06 calculations carried out at GGA optimised geometries are also reported.

The large energy-difference of about ~1.5 eV between the $Fe^{3+}_{A,HS}$ and the $Fe^{3+}_{B,LS}$ atomic configurations using GGA + U is striking, and consistent with previous LDA + U calculations (Hsu et al., 2012). This contrasts with results from GGA calculations (without the use of a +U term), where the $Fe^{3+}_{B,LS}$ configurations are about 0.5 eV higher in energy than the $Fe^{3+}_{A,HS}$ configurations. The $Fe^{3+}_{A,HS}$ and Al tend to cluster together in the first coordination shell at both GGA and GGA + U levels, whereas the $Fe^{3+}_{A,HS}$ configuration with the highest energy has Al and $Fe^{3+}_{A,HS}$ as farthest neighbours within the simulation-box, in agreement with previous GGA calculations (Li et al., 2005b; Stackhouse et al., 2007; Zhang and Oganov, 2006). Our results at the GGA level are in overall agreement with previous GGA calculations carried out by Li et al. (2005b), but they report even smaller energy differences between the $Fe^{3+}_{A,HS}$ and the $Fe^{3+}_{B,LS}$ configurations (of about 0.2 eV).

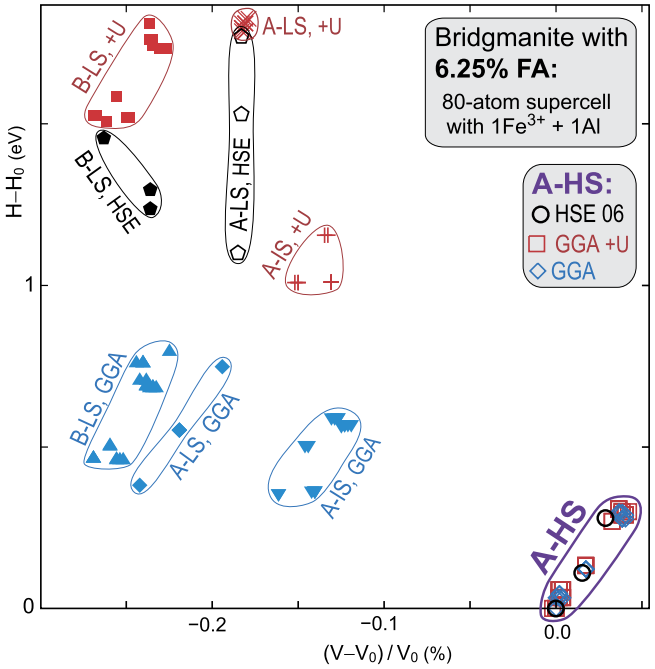

Fig. 1. Optimised cell volume (%) versus minimized enthalpy/simulation cell (eV) for all configurations of Fe^{3+} and Al, calculated in the static limit and 100 GPa with 6.25 mol% FA on the $MgSiO_3$–$FeAlO_3$ (MS–FA) join, using GGA, GGA + U and HSE06 (at GGA geometries) within an 80 ion-unit cell. For HSE06 we calculate the enthalpy for a selection of configurations as discussed in the text. For each of the functionals GGA, GGA + U and HSE06, the configuration with the lowest energy is the reference with $H_0 = 0$ and $V_0 = 0$. Abbreviations: A, B: A- and B-sites; HS, IS, LS: high, intermediate and low spin Fe; +U: GGA + U; HSE: HSE06. Note that many configurations overlap because they are close in energy. The configurations with high-spin Fe^{3+} at the B site (B–HS) are high in energy and not shown. Several $Fe^{3+}_{A,LS}$ configurations optimised using GGA converged to $Fe^{3+}_{A,HS}$, and we sampled only a few datapoints.

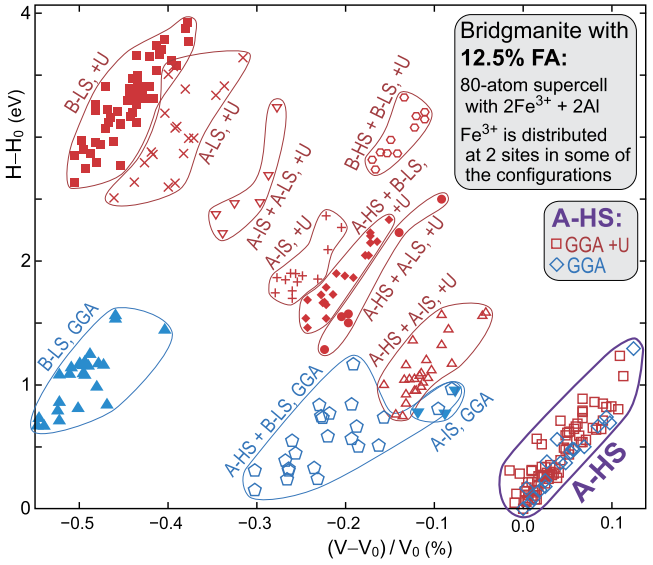

Fig. 2. Optimised cell volume (%) versus enthalpy/simulation cell (eV) for different configurations of Fe^{3+} and Al, computed at the static limit and 100 GPa with 12.5 mol% FA on the $MgSiO_3$–$FeAlO_3$ (MS–FA) join, using GGA and GGA + U. Because the 80-atom cell contains $2Fe^{3+}$ + 2Al, some of the configurations involve Fe on two different sites and with different spin state (as shown in the figure). See Fig. 1 caption for information about zero point definition.

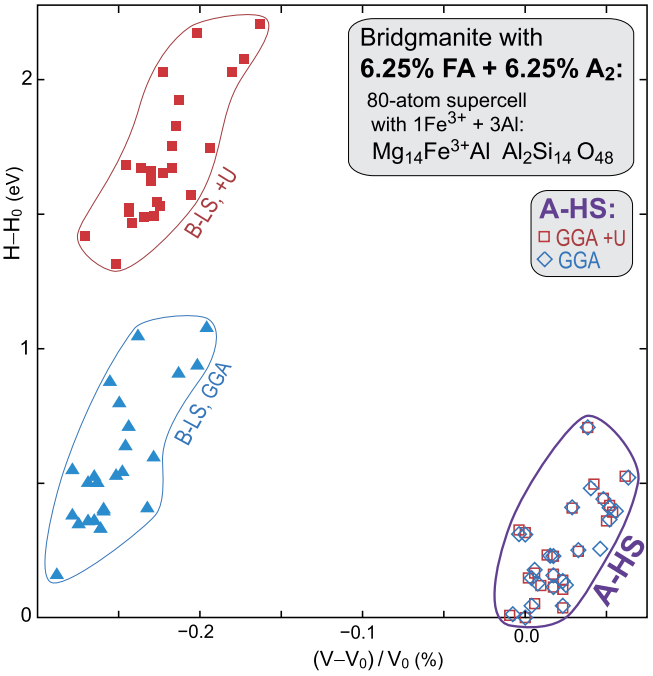

Fig. 3. Optimised cell volume (%) versus enthalpy/simulation cell (eV) for different configurations of Fe^{3+} and Al, computed at the static limit and 100 GPa with 6.25 mol% FA + 6.25 mol% A_2 in the $MgSiO_3$–$FeAlO_3$–Al_2O_3 (MS–FA–A_2) system, using GGA and GGA + U. See Fig. 1 caption for information about zero point definition, abbreviations and the omission of some configurations from the figure.

This small discrepancy is probably either attributable to the different GGA-functionals employed in this work and in Li et al. (2005b) or due to the sampling of the Brillouin-zone, since only the Γ point was included by Li et al. (2005b), whereas we use a 2 × 2 × 2 Monkhorst–Pack.

Discrepancies between GGA and GGA + U are also found when comparing the $Fe^{3+}_{A,IS}$ and $Fe^{3+}_{A,LS}$ configurations. The energies of the $Fe^{3+}_{A,LS}$ and $Fe^{3+}_{A,IS}$ configurations calculated using GGA differ by about 0.4 eV, which again are markedly lower than the corresponding GGA + U results. In general, the IS and LS spin and site-configurations calculated at the GGA level are *always* lower than those of GGA + U which is confirmed by comparing GGA and GGA + U results for bridgmanite with 12.5% FA (Fig. 2) and also by comparing the two functionals for bridgmanite with 6.25% FA + 6.25% A_2 (Fig. 3). The energy difference between the $Fe^{3+}_{A,HS}$ and $Fe^{3+}_{B,LS}$ arrangements calculated using HSE06 is about 1.2–1.5 eV higher than those of GGA, in good agreement with the GGA + U results (Fig. 1).

We analyze the origin of the discrepancy between GGA and GGA + U by decomposing the exchange reaction $Fe^{3+}_{A,HS} + Al_B \rightarrow Fe^{3+}_{B,LS} + Al_A$ in individual contributions as follows:

- spin transition without site-exchange: $Fe^{3+}_{A,HS} + Al_B \rightarrow Fe^{3+}_{A,LS} + Al_B$. This enables us to investigate spurious SIE in GGA which in general favour Fe^{3+}_{LS} over Fe^{3+}_{HS} compared to GGA + U results.
- Site exchange after spin transition: $Fe^{3+}_{A,LS} + Al^{3+}_B \rightarrow Fe^{3+}_{B,LS} + Al^{3+}_A$ enabling a study of weather GGA is capable of handling very different oxygen environment around iron at the A and B sites involving changes in both the crystal fields and covalency of the Fe–O bond.

Conventional LDA and GGA systematically favour low-spin states because energetically favourable correlations between unlike spins (which may be strong in ferric iron) dominates over favourable interactions arising from exchange between parallel spins (Swart, 2004). By contrast, adding an amount of exact Fock-exchange to construct HSE06 may alter this, since Hartree–Fock

Table 1
Boltzmann average Bader charges, deviation from fully ionic character (D), volumes and radii for the different atoms and 80-atoms cell volumes of bridgmanite with 6.25% FA on the MS–FA join, calculated using Eq. (1) at 3000 K and 100 GPa. The Bader radii are calculated from the Bader volumes using $r_{\mathrm{Bader}} = V_{\mathrm{Bader}}^{1/3}$.

	Funct.	q_{Bader} (e)	D (%)	V_{Bader} (Å^3)	r_{Bader} (Å)	V_{cell} (Å^3)
Mg_A^{2+}	+U	+1.72	14	3.71	0.774	
	GGA	+1.72	14	3.71	0.774	
Si_B^{4+}	+U	+3.26	19	2.19	0.649	
	GGA	+3.26	19	2.19	0.649	
Al_A^{3+}	+U	+2.49	17	2.96	0.718	
	GGA	+2.49	17	2.96	0.718	
Al_B^{3+}	+U	+2.47	18	2.55	0.683	
	GGA	+2.47	18	2.55	0.683	
$Fe^{3+}_{HS,A}$	+U	+1.85	38	6.14	0.916	
	GGA	+1.71	43	6.31	0.924	
$Fe^{3+}_{LS,A}$	+U	+1.57	48	5.87	0.902	
	GGA	+1.44	49	6.14	0.916	
$Fe^{3+}_{LS,B}$	+U	+1.54	49	5.89	0.903	
	GGA	+1.43	52	6.03	0.910	
$O_{Fe_{A,HS}}$	+U	−1.65	18	8.83	1.033	521.0
	GGA	−1.64	18	8.81	1.033	520.2
$O_{Fe_{A,LS}}$	+U	−1.64	18	8.79	1.032	518.8
	GGA	−1.64	18	8.78	1.031	518.6
$O_{Fe_{B,LS}}$	+U	−1.64	18	8.79	1.032	519.3
	GGA	−1.64	18	8.78	1.031	518.9

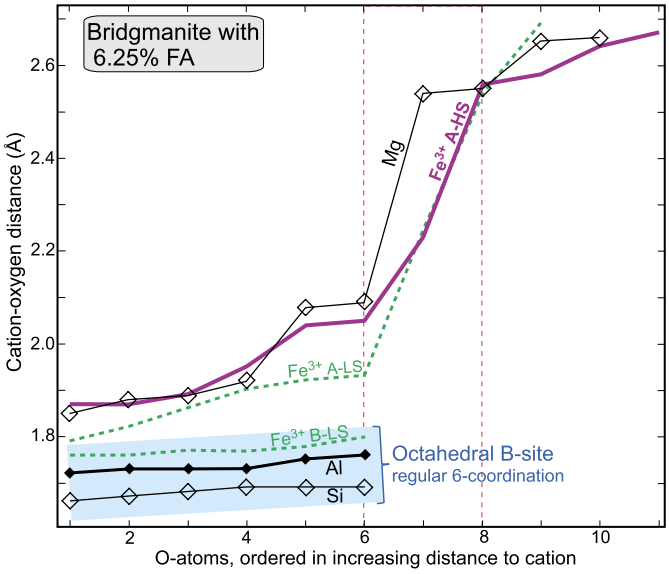

Fig. 4. Average cation–oxygen distances in bridgmanite with 6.25 mol% FA on the $MgSiO_3$–$FeAlO_3$ (MS–FA) join at the static limit and 100 GPa. The A-site coordination is irregular and the closest 9–11 oxygens are shown.

(HF) itself does not describe favourable correlations between unlike spins. The exchange correlation between like spins, however, is treated exactly in HF theory. Because there are 10 favourable exchange interactions of high spin Fe^{3+} and only 4 favourable exchange correlations of low spin Fe^{3+}, HF itself will always favour HS over IS and LS spin states, a property which is often inherited in hybrid-functionals such as HSE06. Reiher et al. (2001) suggested that a lower amount of HF exchange of 15% in B3LYP (a popular hybrid functional frequently used to model molecular systems) performed better in modeling spin-state splittings of iron-complexes. To check if HSE06 is sensitive to the amount of HF exchange, we carried out additional test calculations using HSE06 with only 15% HF exchange, consistent with Reiher et al. (2001). The test calculations show that reducing the amount of HF exchange to 15% has very little influence on the energy difference between the $Fe^{3+}_{A,HS}$ and $Fe^{3+}_{B,LS}$ configurations. The energy difference was reduced by 0.3 eV when the admixture of Fock-exchange was reduced to 15%, confirming a rational mixing of 25% HF exchange in HSE06.

An overdelocalisation of the 3d electrons at the GGA level could influence structural relaxation and in turn the relative stabilization of the $Fe^{3+}_{A,HS}$ configuration compared to $Fe^{3+}_{B,LS}$. As discussed above, a "GGA ion" is larger than a "GGA + U ion" and may therefore "fit" better in the smaller B site, reducing the overall strain and decreasing the energy-difference between the $Fe^{3+}_{B,HS}$ and $Fe^{3+}_{A,HS}$ arrangements. As shown in Figs. 1–3 and Table 1, the GGA $Fe^{3+}_{B,LS}$ ion is only marginally smaller than the GGA + U $Fe^{3+}_{B,LS}$ ion. To analyze if this differences in size may influence structural relaxation and therefore the energy difference of the $Fe^{3+}_{A,HS}$ and $Fe^{3+}_{B,LS}$ configurations, we compare the GGA and GGA + U energy-differences between $Fe^{3+}_{A,HS}$ and $Fe^{3+}_{B,LS}$ configurations carried out at the *same* geometries. The energy difference between the $Fe^{3+}_{B,LS}$ and $Fe^{3+}_{A,HS}$ configurations calculated using GGA + U at *fixed* GGA-optimised geometries is less than 0.2 eV lower than the corresponding energy difference at *fixed* GGA + U-optimised geometries. Therefore, the smaller "GGA + U atom" appears to have very little influence on the relative stability of the HS vs LS configurations.

The local oxygen arrangements around the Fe^{3+}_A and the Fe^{3+}_B are very different, as shown in Fig. 4, where we plot average cation–oxygen distances. Whereas the oxygens around Fe^{3+}_B form a regular octahedron with typical Fe–O bond-lengths of about 1.8 Å, the oxygens around $Fe^{3+}_{A,HS}$ form a markedly distorted polyhedron with six bonds of about 1.9 Å to 2.0 Å and where the next five to six Fe–O distances lie in the range from 2.2 to 2.7 Å. Table 1 shows that the LS Fe–O bonds are in general less ionic than the HS Fe–O bond (Cohen et al., 1997; Swart, 2007). From an ionic point of view, the 3d electrons experience very different crystal fields from the oxygens at the A and B sites. An iron at the B site will experience a strong destabilization of $3d_Z^2$ and $3d_{X^2-Y^2}$ following the $Fe^{3+}_{A,HS} + Al^{3+}_B \rightarrow Fe^{3+}_{B,LS} + Al^{3+}_A$ exchange. To check if these changes affect the relative merits of the GGA, GGA + U and HSE06, we compare the energy difference between, for example, $Fe^{3+}_{B,LS}$ and $Fe^{3+}_{A,LS}$, i.e. the energy difference between iron with the same spin at the two sites. Fig. 1 shows that the energies of the $Fe^{3+}_{B,LS}$ and $Fe^{3+}_{A,LS}$ lie in the same range for each of the functionals.

The discrepancy between the GGA and GGA + U is therefore mainly explained by SIE in the exchange-correlation energy due to changes in the spin-state. The large energy difference between the $Fe^{3+}_{B,LS}$ and $Fe^{3+}_{A,HS}$ configurations calculated using GGA + U and HSE06, suggests that the B site is *not* thermally accessible to Fe^{3+} if $Al > Fe^{3+}$. This contrasts with the popular view where comparison of cation radii taken from e.g. Shannon's compilation (Shannon, 1976), is used to explain the site-preference of Fe^{3+} following the high- to low-spin transition of ferric iron observed in Mössbauer and X-ray experiment (Catalli et al., 2010; Fujino et al., 2012).

The compilation of ionic radii by Shannon (1976) may support the general notion that the configurations with $Fe^{3+}_{A,HS}$ ($r \sim 0.78$ Å) and Al_B ($r \sim 0.535$ Å) is thermodynamically stable in MS–FA-dominated bridgmanites, at least at pressures of the upper to middle parts of the lower mantle. At the higher pressures of the lowermost mantle, however, configurations involving $Fe^{3+}_{B,LS} + Al^{3+}_A$, (with radii of about 0.55 and 0.68 Å, respectively where the Al_A radius is an estimate by Fujino et al., 2012), might be perceived to be volumetrically favourable, although such a site exchange does not lead to a volumetric B-site decrease, according to these simple radius estimates.

Our calculated bond lengths and Bader volumes (Henkelman et al., 2006), presented in Fig. 4 and Table 1, demonstrate that the $Fe^{3+}_{B,LS}$–O bond is longer than the Al^{3+}_B–O bond, and that $Fe^{3+}_{B,LS}$ has a Bader volume and corresponding radius that are 2.3 and 1.3 times

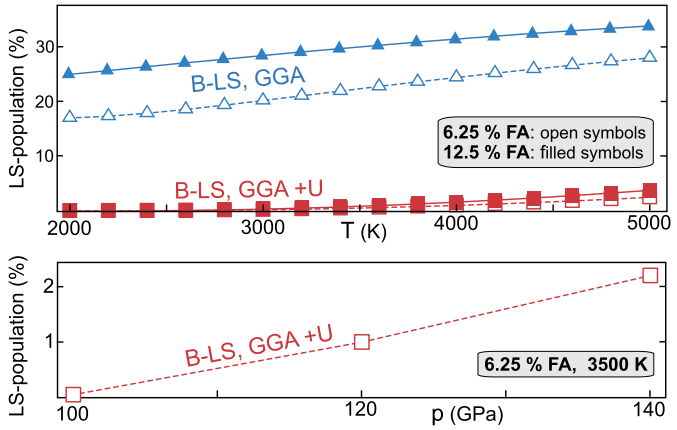

Fig. 5. B-site population of low-spin Fe^{3+} (%) in bridgmanite on the MS–FA join. *Top*: Population versus temperature, calculated using equation (1) at a static pressure of 100 GPa. The total pressures, including the thermal contributions, are approximately 118 and 145 GPa at 2000 and 5000 K, respectively. *Bottom*: Population versus static pressure (100–140 GPa), calculated at 3500 K from equation (1). The corresponding total (static + thermal) pressure range is approximately 132–184 GPa.

those of Al^{3+}_{B}. The Bader size difference between $Fe^{3+}_{A,HS}$ and $Fe^{3+}_{B,LS}$ (GGA + U), however, is very small (4.2 and 1.4% difference in volume and radius, respectively) and the cation-exchange reaction

$$Fe^{3+}_{A,HS} + Al^{3+}_{B} \rightarrow Fe^{3+}_{B,LS} + Al^{3+}_{A} \quad (6)$$

has a volume *increase* of 1.8%, suggesting that B-site substitution of Fe^{3+} remains energetically unfavourable at any pressure. This simple cation-exchange reaction (eq. (6)) does not reflect the contraction of the large O-atoms as a result of charge transfer and the largely covalent nature of the Fe–O bonds, especially those involving $Fe^{3+}_{B,LS}$. Table 1 shows that the deviations from fully ionic character are large for $Fe^{3+}_{A,HS}$ (about 40%) and especially for $Fe^{3+}_{B,LS}$ where the deviation is as large as 50%. To capture the influence on the anions on volume-changes following the spin and site exchange, we look at the full 80-atom cell reaction:

$$(Mg_{15}Fe^{HS})^{A}(AlSi_{15})^{B}O_{48} = (Mg_{15}Al)^{A}(Fe^{LS}Si_{15})^{B}O_{48} \quad (7)$$

which has a small (Bader) volume *decrease* of 0.34% (GGA + U). A volume decrease of about 0.34% is consistent with Fig. 1 and Fig. 2 (compare the cell-volumes of the $Fe^{3+}_{A,HS}$ and $Fe^{3+}_{B,LS}$ configurations) since the sum Bader-volumes gives the total cell-volume.

This indicate that a spin-transition may be favoured at elevated pressure and emphasise that the use of simple concepts such as the comparison of cation radii as a guide to crystal chemical changes at lower mantle conditions is misleading and should generally be avoided. It is essential to include the contractions of the oxygens in analysing the (potential) spin and site-transition, using an appropriate partitioning scheme such as that of Bader (Henkelman et al., 2006). Although ΔV in eq. (7) is negative, extrapolating from static calculations carried out at 100, 120 and 140 GPa, suggests that the spin-transition will take place at pressure >200 GPa, in agreement with LDA + U_{sc} calculations (Hsu et al., 2012).

Fig. 5 shows the populations of the different spins (and sites) calculated using Boltzmann statistics (Eq. (1)) for bridgmanite with 6.25% and 12.5% FA, respectively, derived by averaging over all possible distinct arrangements of Fe^{3+} and Al. At lowermost mantle conditions, less than 1% of the iron are LS and even at extreme temperatures such as 5000 K < 4% of the B site positions are populated at the GGA + U (U = 5) level. Hsu et al. (2012) used a slightly lower value of U in their LDA + U_{sc} calculations, which gives slightly smaller energy-differences between $Fe^{3+}_{A,HS}$ and $Fe^{3+}_{A,LS}$ configurations (by about 0.3 eV), in quantitative agreement with our HSE06 values reported in Fig. 1. To check to what extent lowering the value of +U influence the populations of the HS and LS spin-states, we carried out additional Boltzmann averaging by shifting the distribution of $Fe^{3+}_{B,LS}$ configurations shown in Fig. 1 by 0.3 eV to lower energies. The results from these additional tests show that the population of $Fe^{3+}_{B,LS}$ is 0.7% at 3000 K and about 5% at 5000 K for bridgmanite with 6.25%. By contrast, the GGA results suggest that about 20–30% of the B site positions are populated by Fe^{3+}_{LS} at 3000 K. We do not show the populations of all different spin states of iron in Fig. 5, and only $Fe^{3+}_{A,HS}$, $Fe^{3+}_{B,LS}$ spin configurations are discussed at this point, because we assume that the ions are vibrating within the distinct wells on the Born–Oppenheimer surface (Eq. (1)). This does not allow for electronic excitation, and the summation in eq. (1) measures the site-configurational contribution to the site-population only. That is, at 100 GPa (in the static limit), when the iron-atoms are at the A site, we assume that they *all* possess HS in their electronic ground state, whereas the few that populate the B site (GGA + U) will be LS (since $Fe^{3+}_{B,LS}$ configurations are lower in energy than $Fe^{3+}_{B,HS}$ configurations). However, noting that the $Fe^{3+}_{A,IS}$ is less than 1 eV higher in energy than the $Fe^{3+}_{A,HS}$, and that the magnetic entropy of the IS state is higher than that of HS state due to a higher orbital degeneracy of the former, we can easily modify Eq. (1) to also include electronic IS excitations. The Boltzmann average does therefore not only contain contributions from site-configurations but also contributions from electronic excitations. The inclusion of $Fe^{3+}_{A,IS}$ in the evaluation of Eq. (2) has a small effect on the population of $Fe^{3+}_{A,HS}$. At 3000 K with IS included in the Boltzmann average, about 95% of the iron atoms are $Fe^{3+}_{A,HS}$ and about 5% are $Fe^{3+}_{A,IS}$. The $Fe^{3+}_{A,LS}$ will not contribute since they are all far too high in energy. We do not find any evidence for a high-to-low spin transition in bridgmanite on the MS–FA join within the deep Earth, because GGA + U show that *all* $Fe^{3+}_{B,LS}$ and $Fe^{3+}_{A,LS}$ configurations are high in energy and thermally inaccessible.

4.2. Comparison with experimental results and implications for bridgmanite in the mantle

Bridgmantite crystallizing below and above the solidus in experiments on lherzolitic and basaltic compositions (both natural and simplified, synthetic) is generally characterized by Al/Fe_{total} ratios above unity (Supplementary information). Although iron is present largely as the FA component, various studies have yielded conflicting evidence on the Fe^{3+}–Al site distribution and spin state. Our results indicate that Fe^{3+}_{HS} in bridgmanite in the MS–FA and MS–FA–A_2 systems are confined only to the A site, in the pressure and temperature range of the lowermost mantle (see Fig. 5). Bridgmante in the system $MgSiO_3$–$FeSiO_3$–Al_2O_3–Fe_2O_3 with excess Fe^{3+} relative to Al, or in the system $MgSiO_3$–$FeSiO_3$–Fe_2O_3, must incorporate Fe^{3+} in the B site to maintain charge balance. It seems well established that Fe^{3+}_{B} undergoes a low-spin transition at mid-mantle pressures and temperatures (Catalli et al., 2010; Kupenko et al., 2015; Xu et al., 2015). Several experimental studies support the notion that in bridgmanite with a mole fraction of Al ≥ Fe^{3+}, all of the ferric iron remains in the high-spin state in the A site (e.g. Potapkin et al., 2013; Kupenko et al., 2015). Other investigations of bridgmanite on the MS–FA join, however, have concluded that $Fe^{3+}_{A,HS}$ swap position with Al^{3+}_{B} and undergoes a site-exchange following a spin transition (e.g. Catalli et al., 2011; Fujino et al., 2012).

The reasons for the conflicting experimental observations are not clear, although Hsu et al. (2012) suggested that a $Fe^{3+}_{A,HS} \rightarrow Fe^{3+}_{B,LS}$ transition can explain a volume-reduction of 0.3% as reported by Catalli et al. (2010) if at least 50% of the iron is located

at the B site. This is consistent with the volume-differences between the $Fe^{3+}_{A,HS}$ and $Fe^{3+}_{B,LS}$ configurations in Figs. 1–3. However, the LDA + U calculations reported by Hsu et al. (2012) carried out at 100 GPa and 2100 K, show that about 4% of the ferric iron occupies the B site, which is higher than that found in this study (at both GGA + U = 5 and HSE06 levels of theory). A population of only 4% of the $Fe^{3+}_{B,LS}$ still does not explain the volume-reduction of 0.6% suggested by Catalli et al. (2010). Hsu et al. (2012) explained the discrepancy between their calculated $Fe^{3+}_{B,LS}$ population and the experimental results of Catalli et al. (2010) by their incomplete sampling of the configurational space, overlooking important possible low-energy configurations.

Our results lend very little support to this view, because we investigated all possible configurations of Al and Fe within an 80-ion cell for bridgmanite with 6.25% and 12.5% FA on the MS–FA join and with 6.25% FA + 6.25% A_2 in the MS–FA–A_2 system, and found that none of the LS configurations are thermally accessible even at extreme temperature. For bridgmanite with 6.25% FA we also found the *same* low-energy configurations as Hsu et al. (2012) and Zhang and Oganov (2006) where Al and $Fe^{3+}_{A,HS}$ prefer to cluster together as nearest neighbours. To check if extended Al–Fe clusters can alter the relative stability of the $Fe^{3+}_{A,HS}$ and $Fe^{3+}_{B,LS}$ configurations, we carried out additional calculations at 100 GPa using a larger 360 atoms supercell. In these calculations 8 Al and 8 Fe were distributed such as to maximise the number of Al–Fe nearest-neighbours. In addition we investigated extreme configurations where Fe–Fe are aligned as nearest neighbours (although such configurations are high in energy in the 80-ion calculations), and also selected random configurations. These additional test-calculations carried out in a 360-atom cell, confirm the results from the 80-ion cell that $Fe^{3+}_{B,LS}$ is always high in energy and thermally inaccessible. The $Fe^{3+}_{B,LS}$ configuration is about 30 eV/super cell higher in energy than the $Fe^{3+}_{A,HS}$ configurations with the lowest energy suggesting that the correlation-length is reasonably well captured in an 80-ion cell.

However, it is important to bear in mind that although we find that the B site is thermally inaccessible when $Al/Fe_{total} \geq 1$, iron can be kinetically trapped at the B site depending on sample preparation and synthesis. It is therefore possible that a metastably trapped $Fe^{3+}_{B,LS}$ configuration can, at least partly, explain the spin-transition observed in Mössbauer experiments (Catalli et al., 2011; Fujino et al., 2012, 2014), as well as the increasing Fe_{total}/Mg-ratio in bridgmanite coexisting with ferropericlase at 100–120 GPa and 2300 K in the experimental investigation of the Fe/Mg-partitioning by Sinmyo and Hirose (2013). In these studies gel or glass where used as starting materials, whereas experiments with bridgmanite starting material synthesized in a multianvil press at about 25 GPa showed that *all* iron was $Fe^{3+}_{A,HS}$ (Kupenko et al., 2015; Potapkin et al., 2013). We speculate that gel and glass starting materials might favour trapping of metastable $Fe^{3+}_{B,LS}$.

A possible spin transition is expected to affect the Fe–Mg partitioning between bridgmanite and ferropericlase considerably. The well documented gradual transition to low-spin Fe^{2+} in ferropericlase at 40–80 GPa (e.g. Badro et al., 2003; Fujino et al., 2014) can explain the decrease and increase in the Fe/Mg ratio in coexisting bridgmanite and ferropericlase, respectively, through the upper half of the lower mantle (see compilation in Fig. 4 in Sinmyo and Hirose, 2013). The suggestion of a reversed partitioning trend at 100–120 GPa (Sinmyo and Hirose, 2013) is not consistent with Fujino et al. (2014). Their Fig. 4 indicates that A-site Fe^{2+} in bridgmanite remains high-spin to at least 120 GPa and that the suggested site exchange and low-spin transition of Fe^{3+} occur within the 50–70 GPa range.

Challenges in controlling the iron charge may also explain the lack of agreement between experimental studies. Fujino et al. (2014) pointed out the experimental difficulties in characterization of the samples and suggested that they may contain both ferric and ferrous irons. Even if the starting materials are well characterized in terms of iron oxidation state, the tiny sample volume used in laser-heated diamond anvil cell experiments might be vulnerable to contamination from the surrounding reservoirs of native C (diamond) and mostly Re metal (gasket). The oxidation state of iron might therefore be influenced by redox reactions involving ferric and ferrous oxide, carbonate and metal alloys: e.g. $MgO + Fe_2O_3 + C = MgCO_3 + FeO + Fe$ and $3FeO + Re = ReFe + Fe_2O_3$.

5. Conclusions

We have investigated thousands of different Fe^{3+} and Al configurations of bridgmantite with 6.25% and 12.5% FA followed by a statistical analysis of spin and site populations by configurational Boltzmann averaging together with DFT. Because analysis of bridgmanite crystallized in experiments on peridotitic and basaltic model and natural compositions shows that the Al/Fe^{total} atomic ratio generally exceeds unity, some of the Al will probably partition into the A-site, charge-balanced by Al^{3+} in the B-site, at least in the upper part of the lower mantle. We therefore also investigated bridgmanite with 6.25% FA and 6.25% A_2 which to our knowledge has not been studied computationally.

Comparison of results from GGA, GGA + U and HSE06 (with 25 and 15% HF exchange) suggests that GGA frequently used to explain high- to low-spin transitions observed in several Mössbauer and X-ray emission spectroscopy experiments, accompanied by the site-exchange: $Fe^{3+}_{A,HS} + Al_B \rightarrow Fe^{3+}_{B,LS} + Al_A$ is hampered by spurious self interaction errors in the exchange correlation energy. We find that the main source of the discrepancy between the GGA and the GGA + U and HSE06 results is the large difference in exchange energy of the two spin-states, which is not well captured at the GGA level. There are 10 favourable exchange interactions of high spin Fe^{3+} but only 4 favourable exchange interactions of low spin Fe^{3+}, and GGA will therefore always underestimate the energy difference between the LS and HS configurations. The good agreement between the HSE06 and the DFT + U results is particularly encouraging because they differ fundamentally in how they treat SIE.

We find no evidence for a high- to low-spin transition, followed by a site exchange of ferric iron within fully equilibrated samples of iron-bearing bridgmanite at lowermost mantle conditions when $Al \geq Fe^{3+}$. That is the octahedral B-site is high in energy and thermally inaccessible to Fe^{3+}, consistent with recent Mössbauer experiments (Potapkin et al., 2013; Kupenko et al., 2015). Configurational Boltzmann averaging at 3000 K and 100 GPa shows that about 95% of the iron is HS and located at the A site, whereas about 5% is $Fe^{3+}_{A,IS}$ and less than 1% is $Fe^{3+}_{B,LS}$. Although the volume change following the site and spin exchange is negative at 100 GPa (all $Fe^{3+}_{A,HS}$ configurations are larger than $Fe^{3+}_{B,LS}$ configurations), the flexibility of iron to locally adapt promotes its incorporation in the irregularly coordinated A-site, stabilising $Fe^{3+}_{A,HS}$ over $Fe^{3+}_{B,LS}$.

Depending on sample preparation and experimental conditions, iron might become kinetically trapped at the B site and can therefore undergo a spin transition at high pressure and temperature accompanied by a volume-decrease. Such a volume collapse can be understood by changes in covalency/charge-transfer and "flexible" Fe–O bonds rather than by the release of strain following the exchange of the cations: $Fe^{3+}_{A,HS} + Al_B \rightarrow Fe^{3+}_{B,LS} + Al_A$. Indeed, calculated Bader charges and volumes of the different atoms in bridgmanite at 100 GPa and 3000 K (in the static limit) show that the Fe–O bond is characterized by considerable charge transfer following spin transition and site exchange. The deviation from fully ionic character increases from 38% for $Fe^{3+}_{A,HS}$ to 49% for $Fe^{3+}_{B,LS}$ (GGA + U). Popular concepts based on the comparison of cation radii to understand or predict spin-transition and site-preference

of iron is therefore unsuitable at deep mantle conditions, and the covalent nature of the Fe–O bond must be included in the analysis of such processes.

Because bridgmanite in peridotitic and basaltic lithologies mostly have Al/Fe_{total} ratios above unity, the FA-component is dominant. The crystallographic tendency to disproportionate ferrous iron to Fe^{3+} and Fe^0 is therefore likely to presist throughout the mantle. A lack of Fe^{3+} spin transition in the lowermost mantle indicates that the K_D(Fe/Mg) for bridgmanite–ferropriclase partitioning may remain at about 0.5 down to the D″ zone.

Acknowledgements

The Centre for Earth Evolution and Dynamics is funded by CoE-grant 223272 from the Research Council of Norway. The computing time was provided by the Norwegian metacenter for computational science (NOTUR) through a grant of computing time. We thank the two reviewers and the editor John Brodholt for their useful suggestions.

Appendix A. Supplementary material

Supplementary material related to this article can be found online at http://dx.doi.org/10.1016/j.epsl.2016.02.010.

References

Alfredsson, M., Price, G.D., Catlow, C.R.A., Parker, S.C., Orlando, R., Brodholt, J.P., 2004. Electronic structure of the antiferromagnetic B1-structured FeO. Phys. Rev. B 70, 165111.

Allan, N.L., Barrera, G.D., Fracchia, R.M., Lavrentiev, M.Y., Taylor, M.B., Todorov, I.T., Purton, J.A., 2001. Free energy of solid solutions and phase diagrams via quasi-harmonic lattice dynamics. Phys. Rev. B 63, 094203.

Badro, J., Fiquet, G., Guyot, F., Rueff, J.P., Struzjin, V.V., Vvanko, G., Monaco, G., 2003. Iron partitioning in the Earth mantle: toward a deep lower mantle discontinuity. Science 300, 789–791.

Bakken, E., Allan, N.L., Barron, T.H.K., Mohn, C.E., Todorov, I.T., Stølen, S., 2003. Order–disorder in grossly non-stoichiometric $SrFeO_{2.50}$ – a simulation study. Phys. Chem. Chem. Phys. 5, 2237–2243.

Brodholt, J.P., 2000. Pressure-induced changes in the compression mechanism of aluminous perovskite in the Earth's lower mantle. Nature 407, 620–622.

Catalli, K., Shim, S.-H., Dera, P., Prakapenka, V.B., Zhao, J., Sturhahn, W., Chow, P., Xiao, Y., Cynn, H., Evans, W.J., 2011. Effects of the Fe^{3+} spin transition on the properties of aluminous perovskite—new insights for lower-mantle seismic heterogeneities. Earth Planet. Sci. Lett. 310.

Catalli, K., Shim, S.H., Prakapenka, V., Zaho, V., Sturhahn, W., Chow, W., Xiau, Y., Liu, H., Cynn, H., Evans, W., 2010. X-ray diffraction and Mossbauer spectroscopy of Fe^{3+} bearing Mg-silicate perovskite and its effect on elastic properties. Earth Planet. Sci. Lett. 289, 68–75.

Cococcioni, M., de Gironcoli, S., 2005. Linear response approach to the calculation of the effective interaction parameters in the LDA + U method. Phys. Rev. B 71, 035105.

Cohen, R.E., Mazin, I.I., Isaak, D.G., 1997. Magnetic collapse in transition metal oxides at high pressure: implications for the earth. Science 275, 654–657.

Frost, D.J., Liebske, C., Langenhorst, F., McCammon, C.A., Trønnes, R.G., Rubie, D.C., 2004. Experimental evidence for the existence of iron-rich metal in the Earth's lower mantle. Nature 428, 409–412.

Fujino, K., Nishio-Hamane, D., Nagai, T., Seto, Y., Kunwayama, Y., Whitaker, M., Ohfuji, H., Shinmei, T., Irifune, T., 2014. Spin transition, substitution, and partitioning of iron in lower mantle minerals. Phys. Earth Planet. Inter. 228, 186–191.

Fujino, K., Nishio-Hamane, D., Seto, Y., Sata, N., Nagai, T., Shinmei, T., Irifune, T., Ishii, H., Hiraoka, N., Cai, T., Cai, Y.-Q., Tsuei, K.-D., 2012. Spin transition of ferric iron in Al-bearing Mg-perovskite up to 200 GPa and its implication for the lower mantle. Earth Planet. Sci. Lett. 317–318, 407–412.

Henkelman, G., Arnaldsson, A., Jónsson, H., 2006. A fast and robust algorithm for Bader decomposition of charge density. Compos. Mater. Sci. 36, 354–360.

Heyd, J., Scuseria, G.E., 2004. Efficient hybrid density functional calculations in solids: assessment of the Heyd–Scuseria–Ernzerhof screened Coulomb hybrid functional. J. Chem. Phys. 121, 1187.

Heyd, J., Scuseria, G.E., Ernzerhof, M., 2003. Hybrid functionals based on a screened Coulomb potential. J. Chem. Phys. 118, 8207–8215.

Hofmeister, A.M., 2006. Is low spin Fe^{2+} present in Earth mantle? Earth Planet. Sci. Lett. 243, 44.

Hsu, H., Blaha, P., Cococcioni, M., Wentzcovitch, R.M., 2011. Spin-state crossover and hyperfine interactions of ferric iron in $MgSiO_3$ perovskite. Phys. Rev. Lett. 106, 118501.

Hsu, H., Yu, Y.G., Wentzcovitch, R.M., 2012. Spin crossover of iron in aluminous $MgSiO_3$ perovskite and post-perovskite. Earth Planet. Sci. Lett. 359–360, 34–39.

Huang, D., Pan, Y., 2012. Pressure-induced spin transitions of iron in $MgSiO_3$ perovskite: a GG + U study. High Press. Res. 32, 270–279.

Kresse, G., Joubert, J., 1999. From ultrasoft pseudopotentials to the projector augmented-wave method. Phys. Rev. B 59, 1758–1775.

Kupenko, I., McCammon, C., Sinmyo, R., Cerantola, V., Potapkin, V., Chumakov, A.I., Kantor, A., Rueffer, R., Dubrovinsky, L., 2015. Oxidation state of the lower mantle: in situ observations of the iron electronic configuration in bridgmanite at extreme conditions. Earth Planet. Sci. Lett. 423, 78–86.

Li, L., Brodholt, J.P., Stackhouse, S., Weidner, D.J., Alfredsson, M., Price, G.D., 2005a. Elasticity of (Mg, Fe)(Si, Al)O_3-perovskite at high pressure. Earth Planet. Sci. Lett. 240, 529–536.

Li, L., Brodholt, J.P., Stackhouse, S., Weidner, D.J., Alfredsson, M., Price, G.D., 2005b. Electronic spin state of ferric iron in Al-bearing perovskite in the lower mantle. Geophys. Res. Lett. 32, L17307.

Mao, Z., Lin, J.-F., Yang, J., Wu, J., Watson, H.C., Xiao, Y., Chow, P., Zhao, J., 2014. Spin and valence states of iron in Al-bearing silicate glass at high pressures studied by synchrotron Mössbauer and X-ray emission spectroscopy. Am. Mineral. 99, 415–423.

Mohn, C.E., Allan, N.L., Freeman, C.L., Ravindran, P., Stølen, S., 2005a. Order in the disordered state: local structural entities in the fast ion conductor $Ba_2In_2O_5$. J. Solid State Chem. 178, 346–355.

Mohn, C.E., Lavrentiev, M.Y., Allan, N.L., Bakken, E., Stølen, S., 2005b. Size mismatch effects in oxide solid solutions using Monte Carlo and configurational averaging. Phys. Chem. Chem. Phys. 7, 1127–1135.

Mohn, C.E., Stølen, S., 2005. Genetic mapping of the distribution of minima on the potential energy surface of disordered systems. J. Chem. Phys. 123, 114104.

Ohnishi, S., 1978. A theory of the pressure-induced high-spin–low-spin transition of transition metal oxides. Phys. Earth Planet. Inter. 17, 130–136.

Palme, H., O'Neill, H.St.C., 2003. In: Holland, H.D., Turekian, K.K. (Eds.), The Mantle and Core, vol. 2. Elsevier–Pergamon, Oxford.

Perdew, J.P., Burke, K., Ernzerhof, M., 1996. Generalized gradient approximation made simple. Phys. Rev. Lett. 77, 3865.

Potapkin, V., McCammon, C., Glazyrin, K., Kantor, A., Kupenko, I., Prescher, C., Sinmyo, R., Smirnov, G.V., Chumakov, A.I., Rüffer, R., Dubrovinsky, L., 2013. Effect of iron oxidation state on the electrical conductivity of the Earths lower mantle. Nat. Commun. 1427, 4.

Pozun, Z.D., Henkelman, G., 2011. Hybrid density functional theory band structure engineering in hematite. J. Chem. Phys. 134, 224706.

Reiher, M., Salomon, O., Hess, B., 2001. Reparameterization of hybrid functionals based on energy differences of states of different multiplicity. Theor. Comput. Sci. 107 (1), 48–55.

Rohrbach, A., Ballhaus, C., Golla-Schindler, U., Ulmer, P., Kamenetsky, V.S., Kuzmin, D.V., 2007. Metal saturation in the upper mantle. Nature 449, 456–458.

Rollmann, G., Rohrbach, A., Entel, P., Hafner, J., 2004. First-principles calculation of the structure and magnetic phases of hematite. Phys. Rev. B 69.

Shannon, R.D., 1976. Revised effective ionic radii and systematic studies on interatomic distances in halids and calcogenides. Acta Crystallogr. A32, 751–767.

Sinmyo, R., Hirose, K., 2013. Iron partitioning in a pyrolytic lower mantle. Phys. Chem. Miner. 40, 107–113.

Stackhouse, S., Brodholt, P., Price, G.D., 2007. Electronic spin transitions in iron-bearing $MgSiO_3$ perovskite. Earth Planet. Sci. Lett. 253, 282–290.

Stølen, S., Bakken, E., Mohn, C.E., 2006. Oxygen-deficient perovskites: linking structure, energetics and ion transport. Phys. Chem. Chem. Phys. 8, 429.

Swart, M., 2004. Why DFT favours low-spin. J. Phys. Chem. A 108, 5479–5483.

Swart, M., 2007. Metal-ligand bonding in metallocenes: differentiation between spin state, electrostatic and covalent bonding. Inorg. Chim. Acta 360, 179–189.

Todorov, I.T., Allan, N.L., Lavrentiev, M.Y., Freeman, C.L., Mohn, C.E., Purton, J.A., 2004. Simulation of mineral solid solutions at zero and high pressure using lattice statics, lattice dynamics and Monte Carlo methods. J. Phys. Condens. Matter 16, S2751.

Togo, A., Oba, F., Tanaka, I., 2008. First-principles calculations of the ferroelastic transition between rutile-type and $CaCl_2$-type SiO_2 at high pressures. Phys. Rev. B 78, 134106.

Tsuchiya, J., Tsuchiya, T., Wentzcovitch, R.M., Allen, P.B., 2005. Vibrational and thermodynamic properties of $MgSiO_3$ postperovskite. J. Geophys. Res. 110, 2204.

Ulbrich, H.H., Waldbaum, D.R., 1976. Structural and other contributions to the third low entropies of silicates. Geochim. Cosmochim. Acta 40, 1.

Vanpeteghem, C., Angel, R., Ross, N., Jacobsen, S., Dobson, D., Litasov, K., Ohtani, E., 2006. Al, Fe substitution in the $MgSiO_3$ perovskite structure: a single-crystal X-ray diffraction study. Phys. Earth Planet. Inter., 96–103.

Walter, M.J., Trønnes, R.G., Armstrong, L.S., Lord, O.T., Caldwell, W.A., Clark, S.M., 2006. Subsolidus phase relations and perovskite compressibility in the system $MgO–AlO_{1.5}–SiO_2$ with implications for Earth's lower mantle. Earth Planet. Sci.

Lett. 248 (1–2), 77–89.
Wentzcovitch, R.M., Justo, J.F., Wu, Z., da Silva, C.R.S., Yuen, D.A., Kohlstedt, D., 2009. Anomalous compressibility of ferropericlase throughout the iron spin cross-over. Proc. Natl. Acad. Sci. USA 106, 8447–8452.
Xu, S., Shim, S.-H., Morgan, D., 2015. Origin of Fe^{3+} in Fe-containing, Al-free mantle silicate perovskite. Earth Planet. Sci. Lett. 409, 319–328.
Zhang, F., Oganov, A.R., 2006. Valence state and spin transitions of iron in Earth's mantle silicates. Earth Planet. Sci. Lett. 249, 436.

Iron spin state and site distribution in $FeAlO_3$-bearing bridgmanite
C.E. Mohn and R.G. Trønnes

Supplementary information

Crystal chemistry of bridgmanite in mantle rocks

This supplementary information summarizes the importance of the $FeAlO_3$ and Al_2O_3 components in bridgmanite in mantle rocks. The Al/Fe^{total} ratios of bridgmantite crystallized from peridotitic and basaltic lithologies, both below and above the solidus, are generally above unity (Kesson et al. 1994; 1998; Hirose et al. 1999, 2005; Ono et al. 2001; Hirose, 2002; Hirose & Fei, 2002, Trønnes and Frost, 2002; Frost et al. 2004; Liebske et al. 2005; Murakami et al. 2005; Ricolleau et al. 2010; Irifune et al. 2010; Sinmyo et al., 2011; Sinmyo and Hirose, 2013; Pradhan et al. 2015). With cation sums normalised to 200, the average contents of Al and Fe^{total} are 9 and 8 in peridotitic and 37 and 25 in basaltic compositions, respectively. Additional analyses of the Fe^{3+}/Fe^{total} ratio in bridgmanite crystallized in peridotite and basalt compositions and simplified synthetic compositions with variable proportions of Fe and Al (e.g. Lauterbach et al. 2000; Frost and Langenhorst, 2002, Frost et al., 2004; Sinmyo & Hirose, 2011), demonstrate that iron is present dominantly as the $FeAlO_3$ component. A positive correlation between the proportions of Al and Fe^{3+} (e.g. Fig. 5 in Sinmyo and Hirose, 2011) indicates that $FeAlO_3$ may become the only iron component in basaltic bridgmanites with more than 20 Al cations per 200 cation formulas. Our results show that the $Fe^{3+}_{A,HS}$ + Al_B configuration persists for this component through the entire lower mantle. The excess Al relative to Fe^{3+} in bridgmanite will be distributed nearly equally between the A and B sites. Redistribution of Al and Fe^{3+} between the A and B sites accompanied by Fe^{3+} spin pairing is energetically unfavourable also also for bridgmanites with Al-excess (Fig. 3).

Suggestions that the incorporation of trivalent cations in the B site of bridgmanite could be accompanied by oxygen vacancies (Navrotsky et al., 2003) are not supported by the experiments of Walter et al. (2006), indicating that compositions on the $MgSiO_3$-$MgAlO_{2.5}$ join break down to periclase coexisting with bridgmanite on the $MgSiO_3$–Al_2O_3 join (e.g. $Mg_5Al_2Si_3O_{14}$ = 2 MgO + $Mg_3Al_2Si_3O_{12}$). This finding agrees with atomistic simulations by Brodholt (2000) and Akber-Knutson and Bukowinski (2004), who concluded that oxygen-vacancies in bridgmantite are energetically unfavourable at high pressures. The solubility of the Al_2O_3 component in $MgSiO_3$-based bridgmanite is about 25%, corresponding to the pyrope composition (Walter et al. 2006). Based on analyses of bridgmanite crystallized from basaltic bulk compositions (e.g. Kesson et al. 1994; Ono et al. 2001; Hirose & Fei, 2002; Hirose et al. 2005; Ricolleau et al. 2010; Pradhan et al. 2015) and from the composition $Mg_3FeAlSi_3O_{12}$ (Nishio-Hamane et al. 2005), the solubility of the $FeAlO_3$ component may also be close to 25%.

Xu et al. (2015) suggested that bridgmanite in depleted harzburgite, as well as in the upper parts of the lower mantle where garnet occurs as an additional phase, will have low Al/Fe^{total} ratio, significantly below unity. The incorporation of Fe^{3+}_A in bridgmanite is promoted mainly by the the crystal-chemical need for charge balancing the trivalent Al, which partitions preferentially to the B site (Frost et al. 2004, Vanpetegem et al. 2006). Very low bulk rock Al/Fe^{total} ratio may therefore lead to bridgmanite compositions with low Fe^{3+}/Fe^{2+} ratios and low

contents of a separate Fe-dominated metal phase (Fe-Ni-S-alloy phase, e.g. Frost et al. 2004) in the rock. Bridgmanite in lithologies with high Fe^{2+} and low Al, e.g. Fe-rich peridotite cumulates, may undergo transition to low-spin $Fe^{2+}{}_{A}$ in the lowermost mantle (e.g. Badro et al. 2004; Badro 2014). This would potentially increase the partitioning of Fe to bridgmanite, coexisting with ferropericlase towards the core-mantle boundary. Charge-balanced configurations with $Fe^{3+}{}_{A,HS}$ + $Fe^{3+}{}_{B,LS}$ (Xu et al. 2015) or Al_A + $Fe^{3+}{}_{B,LS}$ (Sinmyo and Hirose, 2013; Fujino et al, 2014) are less likely to cause a similar partitioning behaviour.

The occurrence of bridgmanite with low Al/Fe^{total} ratios is unlikely in ordinary peridotite and basalt, even in the presence of coexisting garnet in peridotite in the uppermost lower mantle or in the presence of a coexisting Al-rich phase in basalt in the entire lower mantle. Hirose (2002) presented high quality EMPA analyses of ten bridgmanite assemblages, five with and five without coexisting garnet, from subsolidus peridotite experiments at uppermost lower mantle conditions. The average Al/Fe^{total} ratios of the bridgmanites are quite similar in the two types of assemblages: 0.96 in those with garnet and 1.02 in those without garnet. The basaltic bridgmanites coexisting with Al-rich phases throughout the lower mantle (the hexagonal NAL or the orthorhombic Ca-ferrite structured phases, close to the $NaAlSiO_4$-$MgAl_2O_4$ join) have considerably higher Al/Fe^{total} ratios, averaging 1.5 (see discussion above).

Melt extraction from depleted residues dominated by olivine and orthopyroxene (harzburgite) in the upper mantle will result in decreasing residual Al/Fe ratio because the bulk residue has fairly constant Fe content even at relatively extensive depletion, whereas Al becomes more depleted. The residual Mg/Si and (Mg+Fe)/Si ratios will increase after shallow extraction of basaltic melts. However, extensive Hadean melt depletion in the lower mantle, possibly combined with (early) cumulate crystallization, may not alter the residual Al/Fe ratio much, due to strong Fe-partitioning to the melt (Nomura et al. 2011; Tateno et al. 2014; Pradhan et al. 2015). The value of $K_D{}^{bridgmanite/melt}$(Fe/Mg) is 0.3–0.4 and about 0.1 at pressures below and above 60-80 GPa, respectively. The Mg/Si ratio is not fractionated significantly between a peridotitic residue and a slightly less or slightly more magnesian melt in the transition zone and lower mantle (Liebske and Frost 2012; de Koker et al. 2013). Depleted harzburgites with high Mg/Si-ratio after shallow extraction of basaltic magmas, however, will have higher proportions of ferropericlase with Fe/Mg ratio exceeding that of bridgmanite (e.g. Irifune et al. 2010). This will increase the Al/Fe ratio in bridgmanite and the combined effects might be to minimize a reduction of the Al/Fe-ratio in residual mantle lithologies.

References

Akber-Knutsen, S., Bukowinski, M.S.T., 2004. The energetics of aluminum solubility into $MgSiO_3$ perovskite at lower mantle conditions, Earth Planet. Sci. Lett. 220, 317–330.

Badro, J., 2014. Spin transition in mantle minerals. Ann. Rev. Earth Planet. Sci. 42, 231-248.

Badro, J., Rueff, J.P., Vanko, G., Monaco, G., Fiquet, G., Guyot, F., 2004. Electronic transitions in perovskite: possible nonconvecting layers in the lower mantle. Science 305, 383-386.

Brodholt, J.P., 2000. Pressure-induced changes in the compression mechanism of aluminous perovskite in the earth's mantle. Nature 407, 620–622.

de Koker, N., Karki, B.B., Stixrude, L., 2013. Thermodynamics of the MgO–SiO2 liquid system in Earth's lowermost mantle from first principles. Earth Planet. Sci. Lett. 361, 58–63.

Frost, D. J., Langenhorst, F., 2002. The effect of Al_2O_3 on Fe-Mg partitioning between magnesiowüstite and magnesium silicate perovskite. Earth Planet. Sci. Lett., 199, 227–241.

Frost D.J., Liebske C., Langenhorst F., McCammon C.A.,Trønnes R.G., Rubie D.C., 2004. Experimental evidence for the existence of iron-rich metal in the Earth's lower mantle. Nature 428, 409–12.

Fujino, K., Nishio-Hamane, D., Nagai, T., Seto, Y., Kunwayama, Y., Whitaker, M., Ohfuji, H., Shinmei, T., Irifune, T., 2014. Spin transition, substitution, and partitioning of iron in lower mantle minerals. Earth. Planet. Sci. Lett. 228, 186.

Hirose, K., Fei, Y., Ma, Y., Mao, H.K., 1999. The fate of subducted basaltic crust in the Earth's lower mantle. Nature 397, 53–56.

Hirose, K., 2002. Phase transitions in pyrolitic mantle around 670-km depth: implications for upwelling of plumes from the lower mantle. J. Geophys. Res. 107, B42078.

Hirose, K., Fei, Y., 2002. Subsolidus and melting phase relations of basaltic composition in the uppermost lower mantle. Geochim. Cosmochim. Acta 66, 2099-2108.

Hirose, K., Takafuji, N., Sata, N., Ohishi, Y. 2005. Phase transition and density of subducted MORB crust in the lower mantle. Earth Planet. Sci. Lett. 237, 239–251

Irifune, T., Shinmei, T., MvCammon, C., Miyajima, N., Rubie, D.C., Frost, D.J., 2010. Iron partitioning and density changes of pyrolite in Earth's lower mantle. Science 327, 193-195.

Kesson, S.E., Fitz Gerald J.D., Shelley J.M., 1994. Mineral chemistry and density of subducted basaltic crust at lower-mantle pressures. Nature 372, 767–769.

Kesson, S.E., Fitz Gerald J.D., Shelley J.M., 1998. Mineralogy and dynamics of a pyrolite lower mantle. Nature 393, 252–255.

Liebske, C., Corgne, A., Frost, D.J., Rubie, D.C., Wood, B.J., 2005. Compositional effects on element partitioning between Mg-silicate perovskite and silicate melts. Contrib. Mineral. Petrol. 149, 113–128.

Liebske C., Frost, D.J., 2012. Melting phase relations in the MgO–$MgSiO_3$ system between16 and 26 GPa: Implications for melting in Earth's deep interior. Earth Planet Sci Lett 345-348, 159–170.

Lauterbach, S., McCammon, C., van Aken, P., Langenhorst, F., Seifert, F., 2000. Mössbauer and ELNES spectroscopy of $(Mg,Fe)(Si,Al)O_3$ perovskite: A highly oxidized component of the lower mantle, Contrib. Mineral. Petrol., 138, 17–26.

Murakami, M., K. Hirose, N. Sata, and Y. Ohishi (2005), Post-perovskite phase transition and mineral chemistry in the pyrolitic lowermost mantle, Geophys. Res. Lett., 32, L03304, doi:10.1029/2004GL021956.

Navrotsky, A., Schoenitz, M., Kojitani, H., Xu, H.W., Zhang, J.Z., et al. 2003. Aluminum in magnesium silicate perovskite: formation, structure, and energetics of magnesium-rich defect solid solutions. J. Geophys. Res. 108, 2330.

Nishio-Hamane, D., Nagai, T., Fujino, K., Seto, Y., Takafuji, N., 2005. Fe^{3+} and Al solubilities in $MgSiO_3$ perovskite: implication of the $Fe^{3+}AlO_3$ substitution in $MgSiO_3$ perovskite at the lower mantle condition. Geophys. Res. Lett. 32, doi:101029/2005GL023529.

Nomura, R., Ozawa, H., Tateno, S., Hirose, K., Hernlund, J., Muto, S., Ishii, H., Hiraoka, N., 2011. Spin crossover and iron-rich silicate melt in the Earth's deep mantle. Nature 473, 199–202.

Ono, S., Ito, E., Katsura, T., 2001. Mineralogy of subducted basaltic crust (MORB) from 25 to 37 GPa, and chemical heterogeneity of the lower mantle. Earth Planet. Sci. Lett. 190, 57–63.

Potapkin, V., McCammon, C., Glazyrin, K., Kantor ,A., Kupenko, I., Prescher, C., Sinmyo, R., Smirnov, G.V., Chumakov, A.I., Ruffer, R., Dubrovinsky, L. (2013) Effect of iron oxidation state on the electrical conductivity of the Earth's lower mantle. Nature Comm. 4, 1427.

Pradhan, G.K., Fiquet, G., Siebert, J., Auzende, A.-L., Morard, G., Antonangeli, D., Garbarino, G., 2015. Melting of MORB at core-mantle boundary. Earth Planet. Sci. Lett. 431, 247-251.

Ricolleau, A, Perrillat, J.-P., Fiquet, G., Daniel, I., Matas, J., Addad, A., Menguy, N., Cardon, H., Mezouar, M., Guignet, N., 2010. Phase relations and equation of state of a natural MORB: Implications for the density profile of subducted oceanic crust in the Earth's lower mantle. J. Geophys. Res. 115, B08202.

Sinmyo, R., Hirose, K., Muto, S., Ohishi, Y., Yasuhara, A., 2011. The valence state and partitioning of iron in the Earth's lowermost mantle. J. Geophys. Res. 116, B07205.

Sinmyo, R., Hirose, K., 2013. Iron partitioning in pyrolitic lower mantle. Phys. Chem. Mineral. 40, 107-113.

Tateno, S., Hirose, K., Ohishi, Y., 2014. Melting experiments on peridotite to lowermost mantle conditions. J. Geophys. Res. 119, 4684–4694.

Trønnes, R.G., Frost, D.J., 2002. Peridotite melting and mineral-melt partitioning of major and minor elements at 22–24.5 GPa. Earth Planet. Sci. Lett. 197, 117–131.

Vanpeteghem, C.B., Angel, R.J., Ross, N.L., Jacobsen, S.D., Dobson, D., Litasov, K.D., Ohtani, E., 2006. Al, Fe substitution in the $MgSiO_3$ perovskite structure: asingle-crystal X-ray diffraction study. Phys. Earth Planet. Inter.155, 96–103.

Walter, M.J., Trønnes, R.G., Armstrong, L.S., Lord, O.T., Caldwell, W.A., Clarke, S.M., 2006. Subsolidus phase relations and perovskite compressibility in the system MgO-$AlO_{1.5}$-SiO_2 with implications for the Earth's lower mantle. Earth Planet. Sci. Lett. 248, 77-89.

Xu, S., Shim, S.-H., Morgan, D., 2015. Origin of Fe^{3+} in Fe-containing, Al-free mantle silicate perovskite. Earth Planet. Sci. Lett. 409, 319-228.